Trends in advanced sciences and technology

Trends in Advanced Sciences and Technology

Manuscript 1008

Impact of Glottis Area on Airflow Dynamics in the Human Trachea Using a Simplified Stenosis Pipe Model

Amany M. Kamal

Momtaz Sedrak

Abouelmagd Abdelsamie

ORIGINAL STUDY

Impact of Glottis Area on Airflow Dynamics in the Human Trachea Using a Simplified Stenosis Pipe Model

Amany Mahmoud Kamal*, Momtaz Sedrak, Abouelmagd Abdelsamie

Department of Mechanical Power Engineering, Faculty of Engineering, Mataria, Helwan University, Cairo, Egypt

Abstract

A complex transitional flow is produced in the larynx during the air inhalation process, pivotal for fundamental comprehension and medical advancements in treatment methodologies. This study delves into the influence of the glottis region using a simplified stenosis pipe geometry, examining two distinct cases: (1) the axisymmetric case and (2) the eccentric case. Reynolds-averaged Navier−Stokes equations incorporting a turbulence model with shear stress transport (SST) $k-\omega$, where intermittency transition activated with steady, Newtonian, and incompressible airflow have been used. The analysis underscores the significant impact of the eccentricity on the velocity by increasing by 0.6% compared with the axisymmetric case, also particularly affecting the airflow jet. Stenosis induces alterations in primary airflow structures contingent upon various levels of eccentricity, marginally bolstering the laryngeal jet intensity at higher degrees of eccentricity. Conversely, it conspicuously impacts the recirculation zone, turbulent kinetic energy, and secondary vortices. Augmented eccentricity escalates the recirculation zone and turbulent kinetic energy with 0.4 m^2/s^2, culminating in an amplified root mean square of axial velocity, an indicator of heightened acoustic source terms compared with the axisymmetric case.

Keywords: Higher eccentricity, Laryngeal airflow, Stenotic pipe, Turbulence

1. Introduction

The human airway is one of the interesting research areas. Since many years ago, public health has been one of the very important topics, particularly after coronavirus disease 2019. It had a negative impact on many sectors and industries. Hence, many researchers are working hard to understand many phenomena and treat pain through innovative solutions.

The human respiratory system's phonation components are intricately linked to support several critical processes, most notably voice production. Human voice production is a complex process that involves the coordinated interaction of various physiological systems (Abdelsamie et al., 2024). The glottal jet plays a crucial role in the phonation system through interaction with the vocal fold. The vorticial structure, which is produced, has an impact on this process (Mihaescu et al., 2007).

Recently, computer simulations have become an increasingly helpful tool for a better understanding of fundamental processes and flow behavior in the human body to treat more specifically individual patients. When it comes to therapeutic planning, numerical simulations can provide insightful information; however, the precision of these simulations is essential for their efficient application (Basri et al., 2016).

Abbreviations: CFD, Computational Fluid Dynamics; DoE, Degree of Eccentricity; DoS, Degree of Stenosis; LRN, Low Reynolds-Number; RANS, Reynolds-Averaged Navier−Stokes; RMS, Root Mean Square; RNG, Renormalization Group; TKE, Turbulent Kinetic Energy [m^2/s^2]; WSS, Wall Shear Stress [Pa].

Received 18 January 2024; revised 15 April 2024; accepted 17 April 2024.
Available online 1 June 2024

* Corresponding author. Fluid Mechanics Lab, Mechanical Power Department, Faculty of Engineering-Mataria, Helwan University, Egypt.
E-mail address: Amany_Mahmoud@m-eng.helwan.edu.eg (A.M. Kamal).

https://doi.org/10.62537/2974-444X.1008

Using high-resolution discretization techniques, the basic principles in a biofluid flow that mimics such configurations have first been studied using a simplified stenotic pipe model to better comprehend this intricate process (Mallinger and Drikakis 2002; Varghese et al., 2007). The cross-sectional variation was regarded as critical to initiating the flow transition. As an extension of a previous experimental investigation (Ahmed and Giddens 1984), numerical simulations were undertaken using the same pipe shape at Reynolds numbers ranging from 400 to 800, where the Reynolds number was based on the pipe diameter (Sherwin and Blackburn 2005). Results from direct numerical simulation (DNS) indicate the development of flow instabilities as a function of the specified Reynolds number. Later, also based on DNS, a global linear stability study revealed that a symmetric flow becomes linearly unstable in an eigenmode while raising the Reynolds number. Over a threshold value of Re, the instability generates non-axisymmetric flow oscillations. Transition happens in connection with the breakup of streamwise hairpin vortices formed by the jet downstream of the stenotic throat (Samuelsson et al., 2015). Recently, Mihaescu et al. (2007) proposed an efficient computational method for the aeroacoustics of a static laryngeal model using large eddy simulations (LES) to forecast the flow patterns and acoustic field in the vocal tract and glottis. Abdelsamie et al. (2024) provided a three-dimensional (3D) stenotic pipe using DNS to simulate flows in a stenotic pipe, either axisymmetric or eccentric, at different Reynolds numbers and found that eccentricity significantly accelerates the transition onset, beginning at Re = 500 as opposed to Re = 750 for the axisymmetric case.

Numerical modeling is a powerful tool to analyze the airflow field, which provides more details of the airflow structures and has become very popular in this research area. The Reynolds-averaged Navier–Stokes equations (RANS) coupled with the low-Reynolds number k-ω turbulence model are the most popular way to predict the laminar, transitional, and turbulent flows in the respiratory system (Longest, et al., 2009). Four turbulence models: (1) low-Reynolds-number (LRN) (k–ϵ, and k–ω), (2) the renormalization group (RNG) k–ϵ and Menter k–ω for internal flow systems inside tubular constrictions were compared and evaluated by Kleinstreuer and Zhang (2003). The LRN k-ω model, which was used to simulate complicated 3D tubular flow and could mimic fully turbulent, transitional, and laminar flows, did a good job of predicting higher turbulence changes. However, the Menter k–ω, RNG k–ϵ, and LRN k–ϵ models could not show how laminar flow behaved at low Reynolds numbers influenced by airway profiles. For example, Choi and Wroblewski (1998) report that the airflow patterns are different with the triangular glottis and the circular glottis. Brouns et al. (2007) also find that different shapes and cross-sectional areas for Pulsatile Flow Waveform and Womersley Number will lead to different airflow fields using RANS simulations. In their study, Xi et al. (2018) say that changing the main flow speed changes the laryngeal jet instability and the formation of vortices. Wang et al. (2022) investigated airflow structures depending on the deformation level using a three-dimensional airway and large eddy simulations (LES) with the Smagorinsky subgrid model and found that increasing airway deformation will produce stronger secondary flow, a smaller recirculation zone, and weaker turbulent kinetic energy. The other group studied airflow structures in the respiratory system using LES and found innovatively that during the expiration phase, a shear layer is formed in the convergence region of the lower lung airway. The shear layer quickly disappears after the airflows enter the tubular region, and the TKE becomes very low. The constriction of the glottis leads to a reversed laryngeal jet and a recirculation zone (Cui et al., 2021).

Complex geometry and numerical input simulation data are a challenge, so we can use a simple configuration in a vocal fold to investigate numerical

Nomenclature

D	diameter of human trachea [cm]
d	diameter of stenosis area [cm]
L	length of the stenosis region [cm]
Q	vortex criterion [dimensionless]
θ	azimuth angle [degrees °]
μ	dynamic viscosity [Pa. s]
ρ	density [kg/m^3]
Re	Reynold number [dimensionless]
k	normalized turbulent kinetic energy [dimensionless]
U	normalized average velocity magnitude [dimensionless]
u	normalized instantaneous velocity magnitude [dimensionless]
u′^{2}, v′^{2}, w′^{2}	root-mean-square components of velocity [m^2/s^2]
U $_{avg}$	inlet velocity magnitude [m/s]

Subscripts

x	axial flow

Superscripts

(′)	fluctuating component

data and flow behavior. The early studies of Yoganathan et al., (1986); Bluestein and Einav (1995) investigated in detail what degree of stenosis causes the flow to become turbulent. Earlier experiments by Ahmed and Giddens (1984) investigated post-stenotic flow in a tube using LDA at a mean Reynolds number of 600 and a Womersley number of 7.5. They found strong turbulence and flow separation downstream of the 75% stenosis. Ding et al. (2021) studied pulsatile flow in a 2D stenosed pipe using PIV experiments with a mean Reynolds number of 1750 and a Womersley number of Wo = 6.15. They used 25, 50, and 75% degrees of stenosis and found increasing turbulent intensities with increasing constrictions. Jain (2020) investigated the transition to turbulence in a purely oscillatory flow with three pulsation frequencies in a pipe with a 75% area reduction in eccentric and axisymmetric configurations. He found that the critical Reynolds number at which the flow transitions to turbulence for a zero-mean oscillatory flow through a stenosis is shown to be nearly tripled in comparison with studies of pulsating unidirectional flow through the same stenosis. Some researchers study the numerical hemodynamic effect in stenotic coronary arteries quite extensively with different parameters (Timofeeva et al., 2022). Results are reported in the hemodynamic indices WSS, OSI, and FFR, and they have demonstrated that the flow deflects away from the model's centerline by an eccentric effect. The behavior of the deflected flow is significantly altered downstream of stenosis. The transverse dimension of the recirculation zone grows with increasing degree of eccentric (DoE), and eccentricity also contributes to the development of secondary flow distal to the stenosis. Others study the generalization of stenotic flow in these two applications: cerebrospinal fluid and the air respiratory system. There are three different parameters to explore the detailed characteristics of flow transition (Jain 2022). The result will be a higher degree of stenosis, and eccentricity causes an earlier transition to turbulence in oscillatory flow. Though already very interesting, these findings must be refined further to better understand the airflow structure and eccentric effect of stenosis pipes on the properties of the flow field.

Yet, the number of studies that investigate the impact of eccentricity on the local flow in a straight, smooth artery (pipe) is limited (Tutty, 1992; Varghese et al., 2007; Griffith et al., 2013; Agujetas et al., 2018; Ferreira et al., 2018; Xie et al., 2018). A range of minor stenosis eccentricities were investigated, and the flow distal to the stenosis was very responsive to them. Only one case of eccentric stenosis was addressed by Varghese et al. (2007), where the research was mainly focused on modeling a transition to turbulent flow in the presence of a modest eccentricity. However, most prior research on stenotic flows assumes that the narrowing happens in an axisymmetric manner, while the influence of eccentric stenosis on the airflow field is still uncertain, as shown in Table 1. In the current work, the shortage (the gap) in the literature will be covered by studying the different degrees of axisymmetric with investigation of a higher DoE = 80% with airflow in the trachea at a low Reynolds number (Re = 500) through measured flow-field parameters such as velocity field, wall shear stress, and turbulent kinetic energy.

2. Computational domain

In the present study, a stenotic pipe model, like the one introduced by Mallinger and Drikakis (2002); Varghese et al. (2007) is utilized. This geometry consists of two sections mimicking the throat area and trachea and has been commonly used in studies involving a simplified stenotic pipe in simulation and experimental works (Ahmed and Giddens 1984; Mallinger and Drikakis 2002; Varghese et al., 2007). The trachea's cross-section is assumed to be circular in this model. Steady inflow (i.e., nonpulsatile inflow) was studied and analyzed through both axisymmetric and eccentric stenosis models.

Geometry dimensions and length (Fig. 1) are similar to that in the work by Abdelsamie et al. (2024); these dimensions ensure that the boundaries do not affect the flow behavior or turbulent behavior. A cosine function that depends on the axial position x defines the baseline stenotic pipe. S (x) is used to determine different cross-section coordinates y and z, indicating the stenosis's shape by

$$S(x) = R\,[1 - s0(1 + \cos\,(2\pi\, x / L))] \tag{1}$$

where L = 2D is the length of the stenosis region; s_0 = 0.25 accomplishes area reduction; and D is the diameter of the non-stenotic pipe.

In the eccentric model, the stenosis axis was moved away from the main vessel axis. The updated y and z coordinates were computed as E (x), the offset, and then

$$E(x) = \frac{1}{10}\, s0\, (1 + cos\, (2\pi\, x / L)) \tag{2}$$

where s_0 = 0.25 for area reduction stenosis used throughout this study, while the azimuth angle is denoted by θ. Cartesian coordinate is obtained by

Table 1. Summary and comparison of the present and previous studies, where the references are given in chronological order by date of publication.

References	Parametric study						
	Domain	Flow condition	Methodology	DoS	DoE	Flow	Re
Ahmed and Giddens (1983)	3D	Steady inflow	Experimental	25%, 50%, 75%	Non	Air	500–2000
Ahmed and Giddens (1984)	3D	Pulsatile inflow	Experimental	25%, 50%, 75%	Non	Air	600
Long et al., (2001)	3D	Pulsatile inflow	URANS	25%, 50%, 75%	Non	Blood	300
Ding et al., (2021)	2D	Pulsatile inflow	Experimental	25%, 50%, 75%	Non	Blood	1750
Mallinger and Drikakis (2002)	3D	Pulsatile inflow	High-resolution discretization techniques	75%	Non	Blood	760–1245
Sherwin and Blackburn (2005)	3D	Steady and Pulsatile	DNS	75%	Non	Air	400–800
Varghese et al., (2007)	3D	Steady and Pulsatile	DNS	75%	5%	Air	500, 1000
Jain (2020)	3D	Pulsatile and oscillating	DNS	75%	5%	Air	1800–2100
Abdelsamie et al. (2024)	3D	Steady inflow	DNS	50%	5%	Air	500–1800
Jain (2022)	3D	Pulsatile and oscillating	DNS	25%, 50%, 60%	5%	Air	1800–2200
Present Study	3D	Steady inflow	RANS	25% and 50%	80%	Air	500

Fig. 1. Profile of axisymmetric stenosis pipe.

Table 2. Dimension details of the computational models used in the present work (all dimensions are in cm).

Description	Case (1) DoS 25%, DoE 0%	Case (2) DoS 50%, DoE 0%	Case (3) DoS 50%, DoE 80%
Diameter of nonstenotic (D)	1	1	1
Diameter of stenotic (d)	0.75	0.5	0.5
Length of stenosis (L = 2D)	2	2	2
Length of the upstream region	4	4	4
Length of the downstream region	12	12	12

Table 3. Mesh independence assessment.

	Number of cells	V_{max} (m/s)	Numerical dissipation, 10^{-3}	Percentage error %
1	124,740	1.3766	2.319	0.23%
2	247,660	1.3775	1.667	0.17%
3	453,050	1.37952	2.029	0.02%
4	694,640	1.3798	0.000	0.00%
5	1,200,000	1.3798	0.000	0.00%
6	1,690,000	1.3798	0.000	0.00%

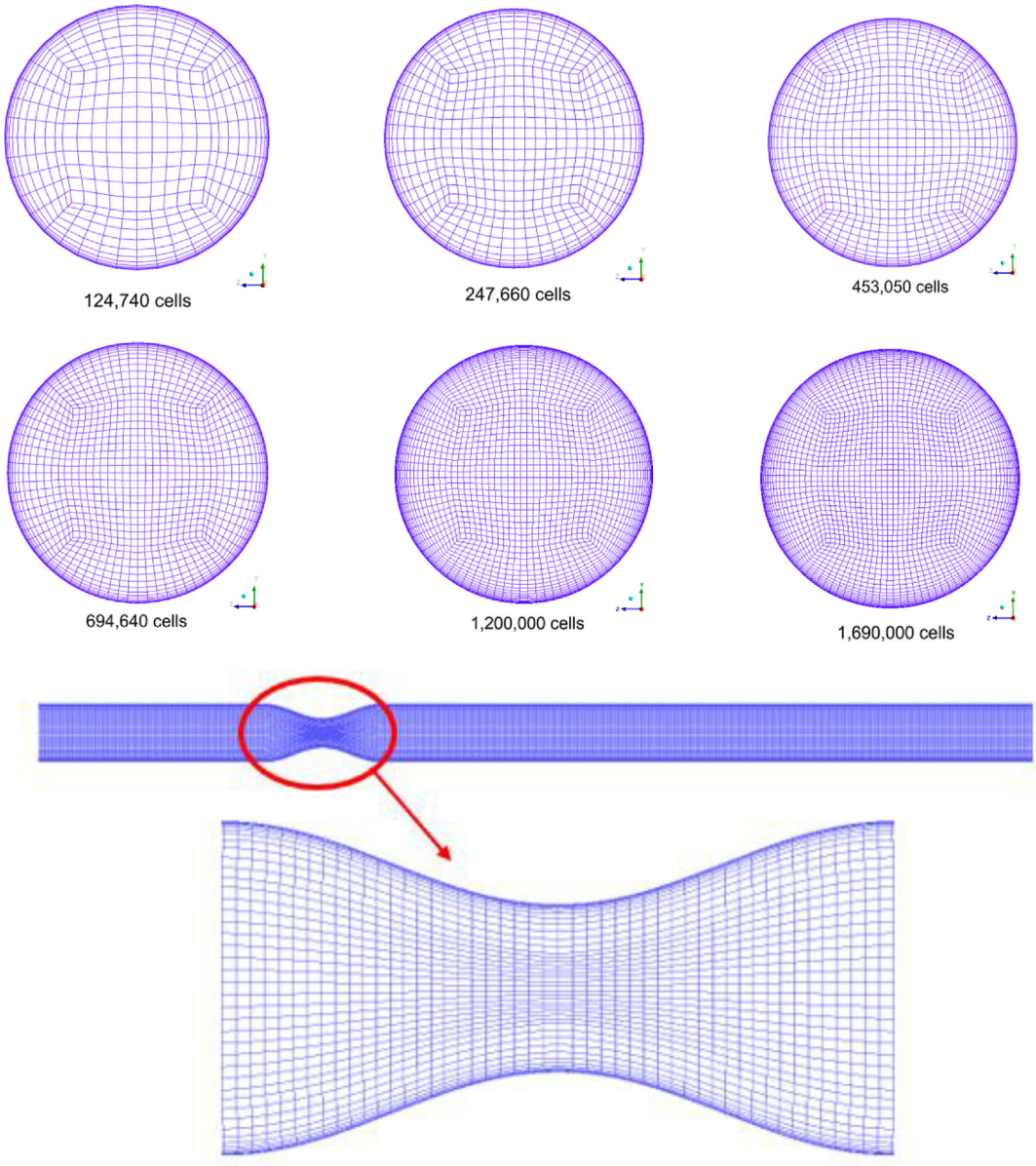

Fig. 2. Structured mesh with (a) y-z plane and (b) x-y plane.

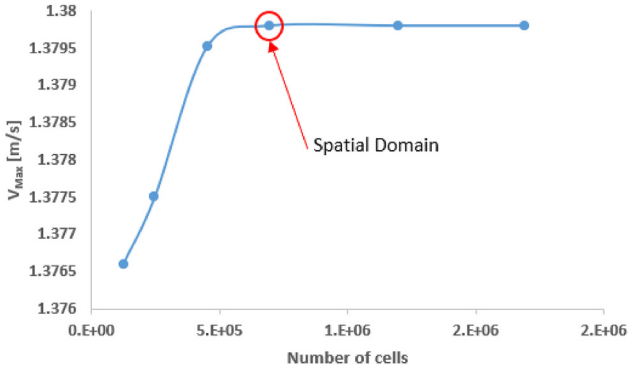

Fig. 3. Mesh independence study.

$$y = S(x) + E(x) \cdot \sin\theta \tag{3}$$

$$z = S(x) \cdot \cos\theta. \tag{4}$$

Measuring from the stenosis throat (x = 0 in Fig. 1), in both models, the vessel's upstream and downstream segments spanned 4 and 12 vessel diameters, respectively. All data of cases are available in Table 2.

2.1. Computational setups and numerical approaches

For all simulations, ANSYS-FLUENT was used with a steady and incompressible flow solver. This

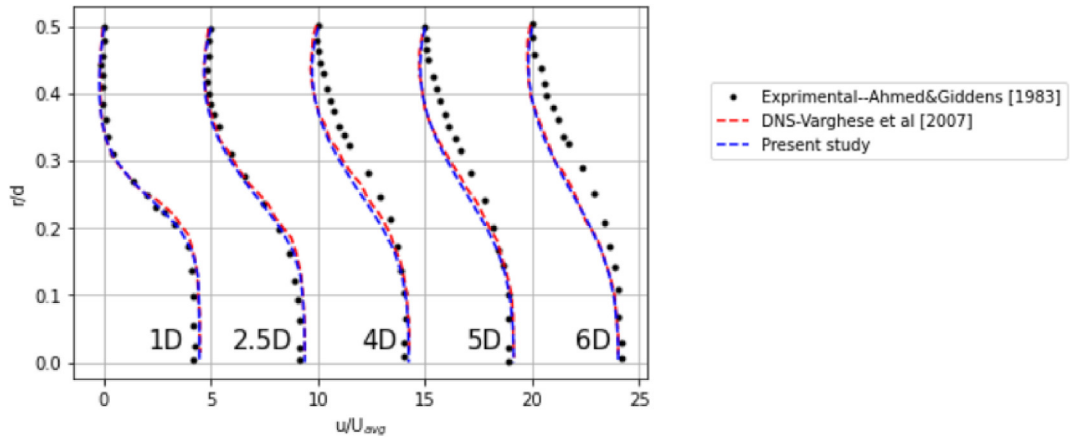

Fig. 4. Model validation.

code was used to solve the steady Navier–Stokes equations based on a finite volume method. In this solver, a pressure–velocity coupling scheme is coupled with the following spatial discretization techniques as (1) second-order pressure discretization, (2) second-order upwind scheme for the momentum equations, and (3) first-order upwind for intermittency, turbulent kinetic energy, and specific

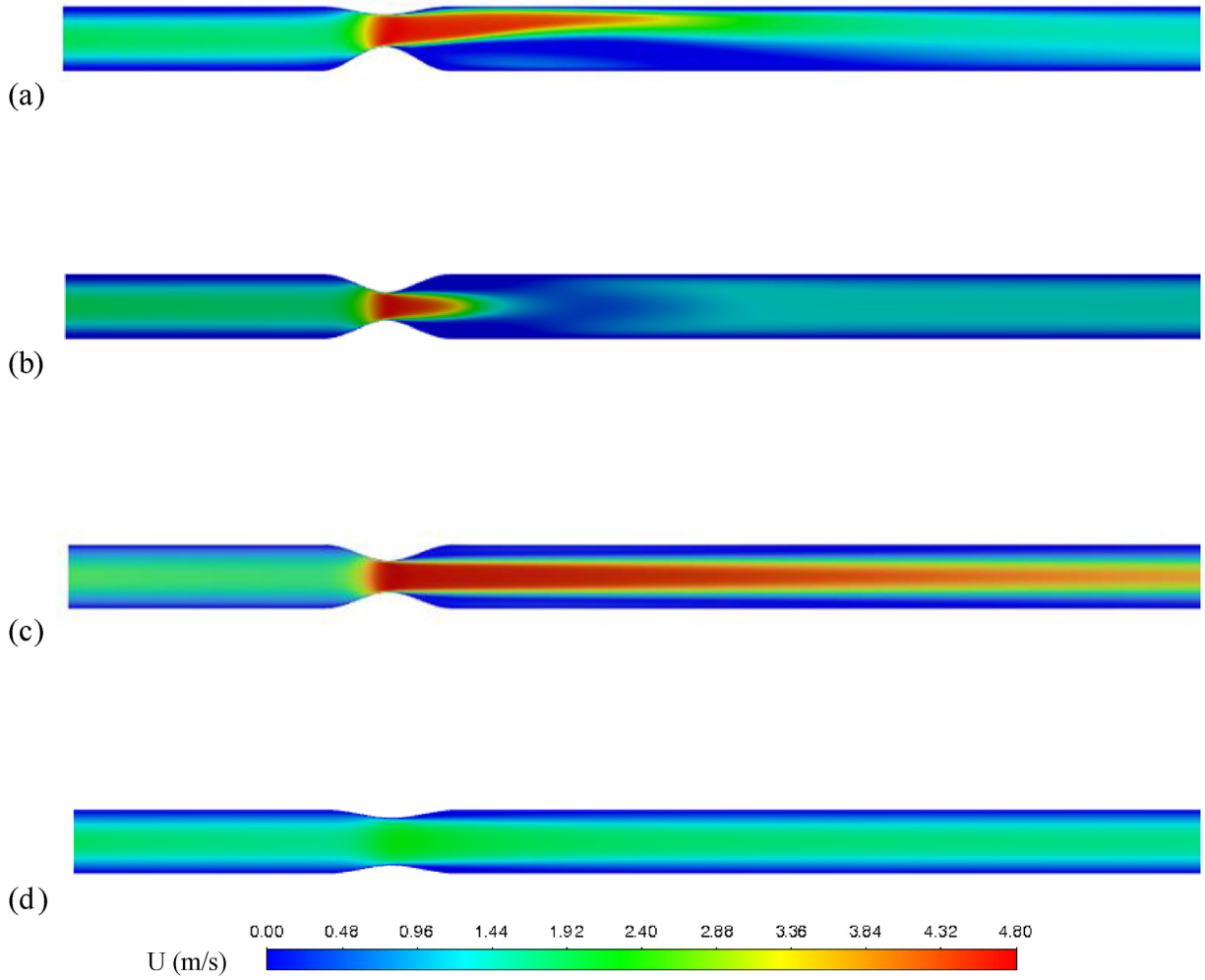

Fig. 5. Temporal-averaged of the velocity magnitude at longitudinal planes of the computational domains: (a) x-y plane of eccentric case, (b) x-z plane of eccentric case, (c) x-y plane of 50% axisymmetric case, and (d) x-y plane of 25% axisymmetric case.

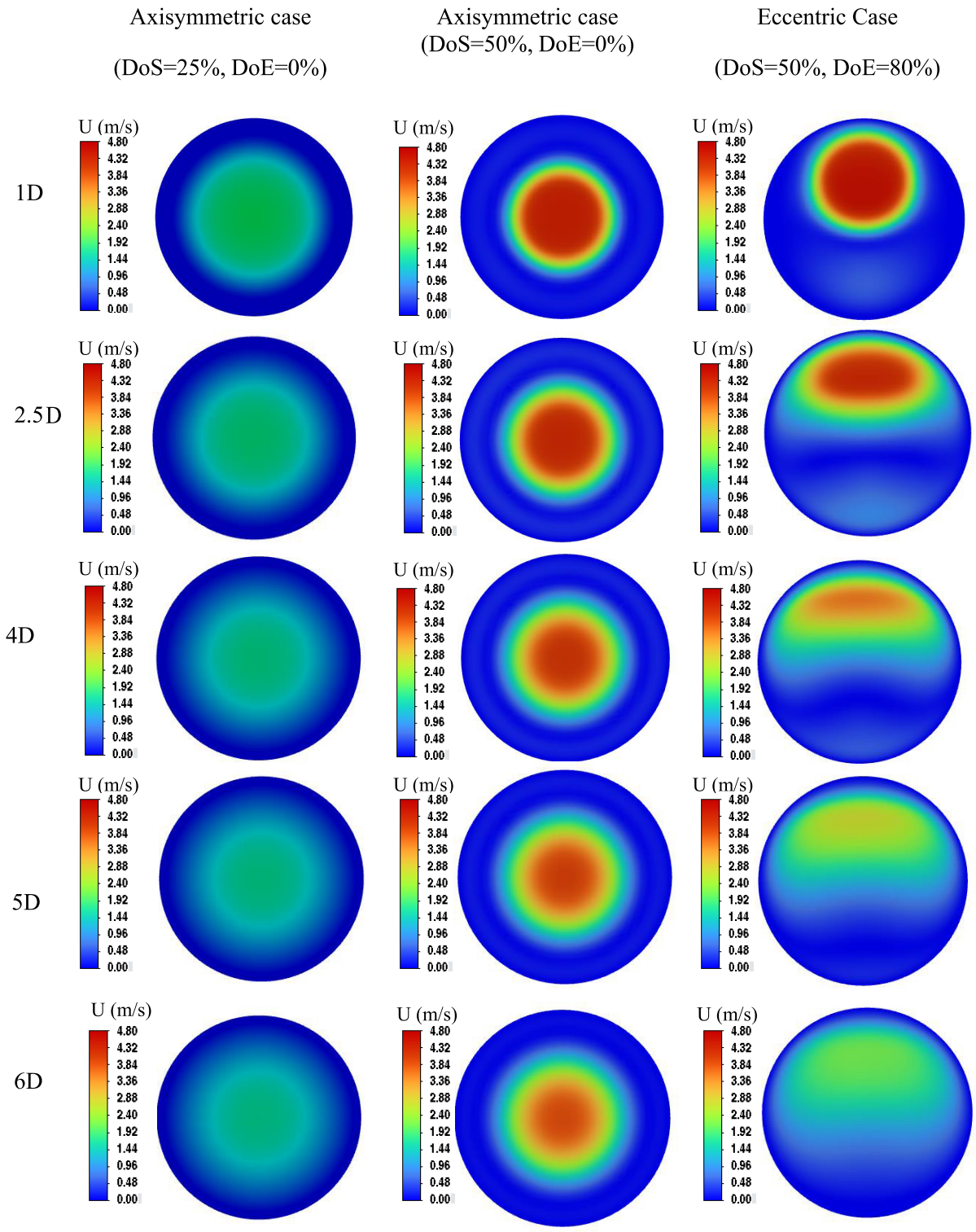

Fig. 6. Time-averaged velocity magnitude at different transverse planes at sections obtained at a distance 1D, 2.5D, 4D, 5D, and 6D from the model's origin (x = 0).

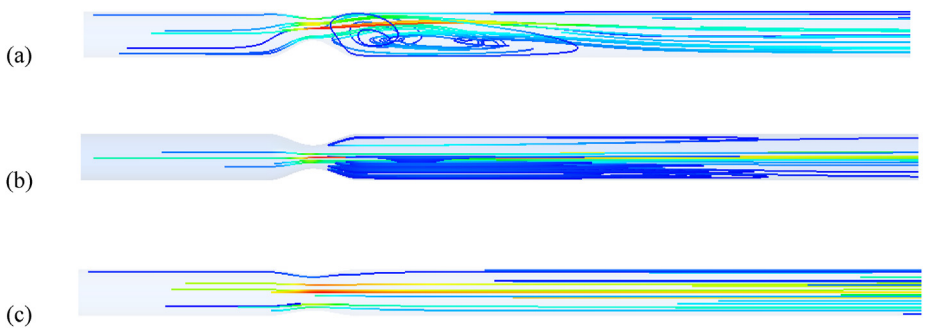

Fig. 7. Isosurface velocity streamlines for three cases. (a) Case (1) eccentric 80%; (b) Case (2) Axisymmetric 50%; and (c) Case (3) axisymmetric 25%.

dissipation rate. This is all activated with a pseudo transition of higher relaxation and hybrid initialization. For the studied geometry (see Fig. 1), the boundary conditions (BC) are inlet velocity (Dirichlet BC for velocity and Neumann BC for pressure) at the left side and pressure-outlet (Neumann BC for velocity and the Dirichlet BC for pressure) at the right side, as referred to by Givoli and Keller (1989); Hughes (1995); Vignon-Clementel et al., (2006). For the turbulence model, SST-K-ω SST-K-ω was used in this study because it is commonly employed in similar works (Kleinstreuer

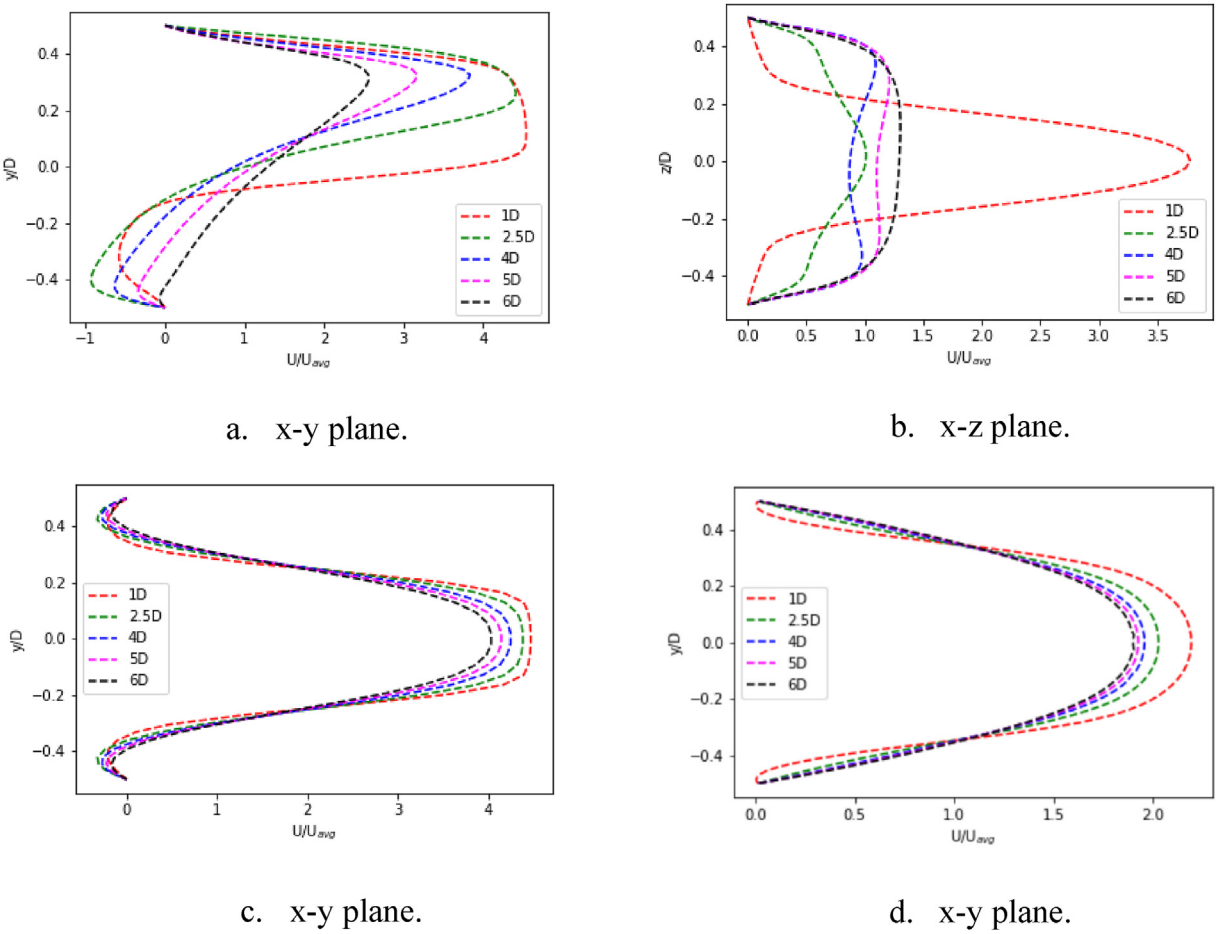

Fig. 8. Temporal-averaged streamwise velocity distribution for eccentric (DoS = 50%, DoE = 80%), axisymmetric (DoS = 50%, DoE = 0%), and axisymmetric (DoS = 25%, DoE = 0%) cases measured at the location of 1D, 2.5D, 4D, 5D, 6D located from the origin of the computational domain (x = 0): (a) eccentric at the x-y plane, (b) eccentric at the x-z plane, (c) axisymmetric case, 50%, and (d) axisymmetric case, 25%.

and Zhang, 2003), which facilitates the validation and comparison. At the inlet, a uniform velocity is implemented as follows:

$$v(r) = 2V\left[1 - \left(\frac{r}{R}\right)^2\right] \quad (5)$$

A laminar inflow from the trachea into the larynx is assumed, and 3.5 l/min of the volume flow rate corresponds to Re = 500. Air is modeled as an incompressible, Newtonian fluid with a dynamic viscosity of 1.7894×10^{-5} Pa• s and a density of 1.225 kg/m^3. All rigid walls have a zero-pressure gradient, and a no-slip velocity condition is applied.

2.2. Mesh topology, mesh independence study, and validation

Structured grids play a vital role in CFD by dividing the domain into well-defined, organized cells, enabling accurate and efficient analysis of fluid flow behavior with a fast convergence rate. Furthermore, the benefit of structured grids lies in their ability to preserve geometric properties, ensuring smooth data interpolation and reliable results. Therefore, the geometry under investigation was discretized into 694,640 hexahedron cells using Ansys ICEM-CFD, as can be seen from Fig. 2.

The mesh independence was judged by comparing the computed velocity along the central line in the geometrical model with centerline velocity at 1,690,000 cells as shown in Table 3. Mesh resolutions were considered adequate. When the mesh density was doubled, velocity was only different by a very small numerical difference as seen from Fig. 3. The centerline velocity of the chosen spatial domain (694,640 hexahedron cells) is 1.3798 m/s, which is an identical value for the reference one. Computational domain discretization is solved by RANS SST-K-ω (Kleinstreuer and Zhang, 2003) and make assessments of the required discretized mesh resolution, and achieved with quality = 65%, orthogonality = 0.664, mass imbalance = 10^{-12}, and y + less than 0.25.

As shown in Fig. 4, the validation of the current models with two different reference data at different line cuts 1D, 2.5D, 4D, 5D, and 6D of the cross-section diameter: (1) experimental work (Ahmed and Giddens 1984) and (2) DNS work (Varghese et al., 2007). As can be observed from Fig. 4, the data from the current simulation agrees very well with the DNS reference data. It is worth noting that the experimental results are obtained as instantaneous values; therefore, the experimental results in Fig. 4 are used as guidance only.

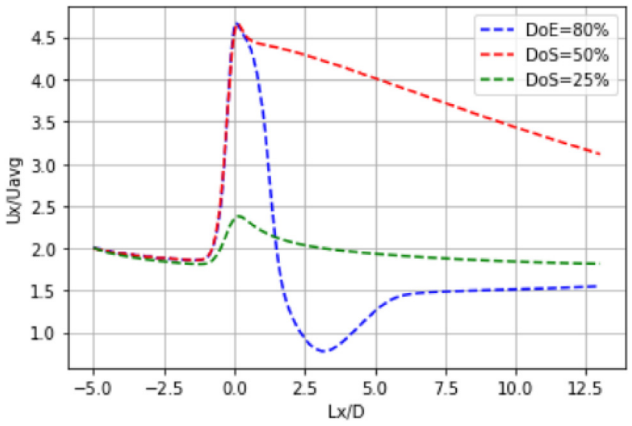

Fig. 9. Normalized mean axial velocity value along the centerline axis of computational domains.

3. Results and discussions

In this section, the data will be presented and discussed in detail. In all results, the velocity, turbulent kinetic energy, and root mean square are normalized by the averaged velocity at the inlet (U_{avg}).

3.1. Flow properties

To investigate the impact of degree of stenosis and higher degree of eccentricity on the flow field, three cases are compared (1) a case with zero degrees of eccentricity, DoE (axisymmetric, DoS = 50%), (2) a case with different construction (axisymmetric,

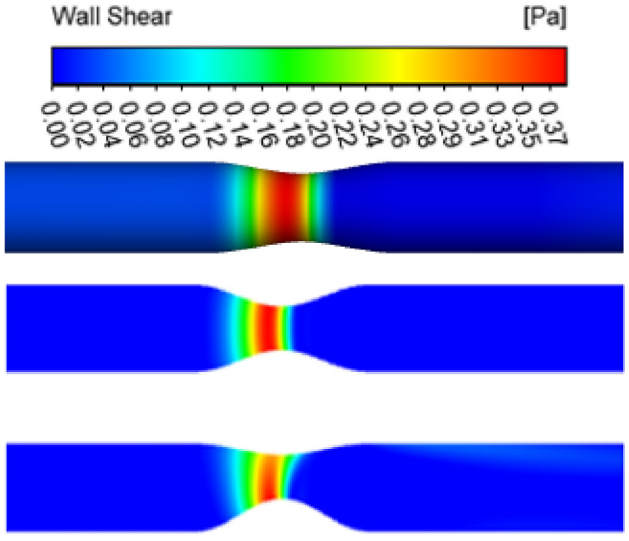

Fig. 10. Color contour of temporal-averaged WSS. Top: axisymmetric case, 25%; Middle: axisymmetric case, 50%; and Bottom: eccentric case, 80%.

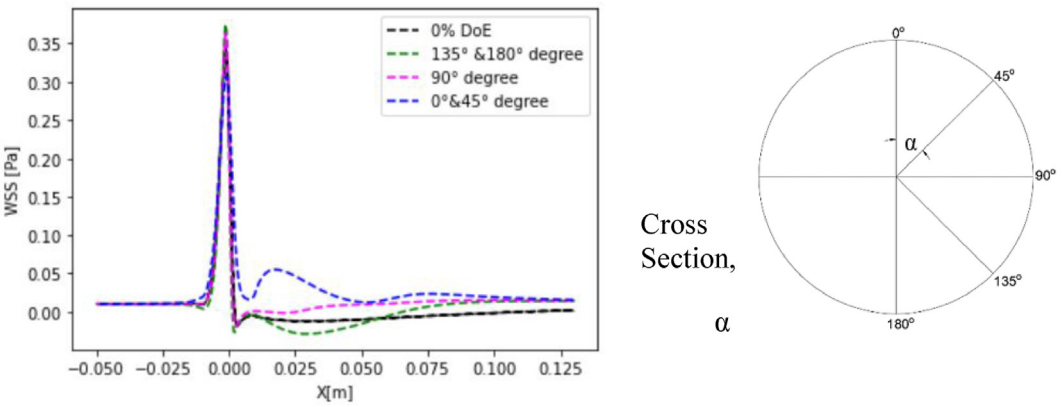

Fig. 11. Axial-direction WSS at a line cut along the streamwise direction of the geometry. For the axisymmetric cases (black dashed line) and the eccentric case (green, pink, and blue) at different circumferential directions, the considered directions are defined to the right of the figure.

DoS = 25%), and (3) a case with a high degree of eccentricity DoE = 80% (eccentric pipe) with keeping the degree of stenosis, DoS = 50% for eccentric case will be examined. The time-averaged velocity magnitude at longitudinal and transverse planes are presented in Fig. 5 and 6, respectively.

In the axisymmetric case, the reverse flow area and velocity profiles have a negative sign as shown in Figs. 5, 6. Once the flow passes through the stenosis area at x = 0, the flow symmetrically reverses close to the walls. Case DoE (DoS = 50%, DoE = 80%) causes a high reverse flow in an eccentric direction. The recirculation zone decreases gradually to absent effect significantly far away from the stenosis at x = 6D in axisymmetric case (DoS = 25%), the flow passes through the stenosis area with a maximum velocity of 1.76 m/s while in the axisymmetric case (DoS = 50%), the flow passes with a maximum velocity of 4.66 m/s. Velocity profiles with a negative sign increases in the axisymmetric case (DoS = 50%). In conclusion, eddy

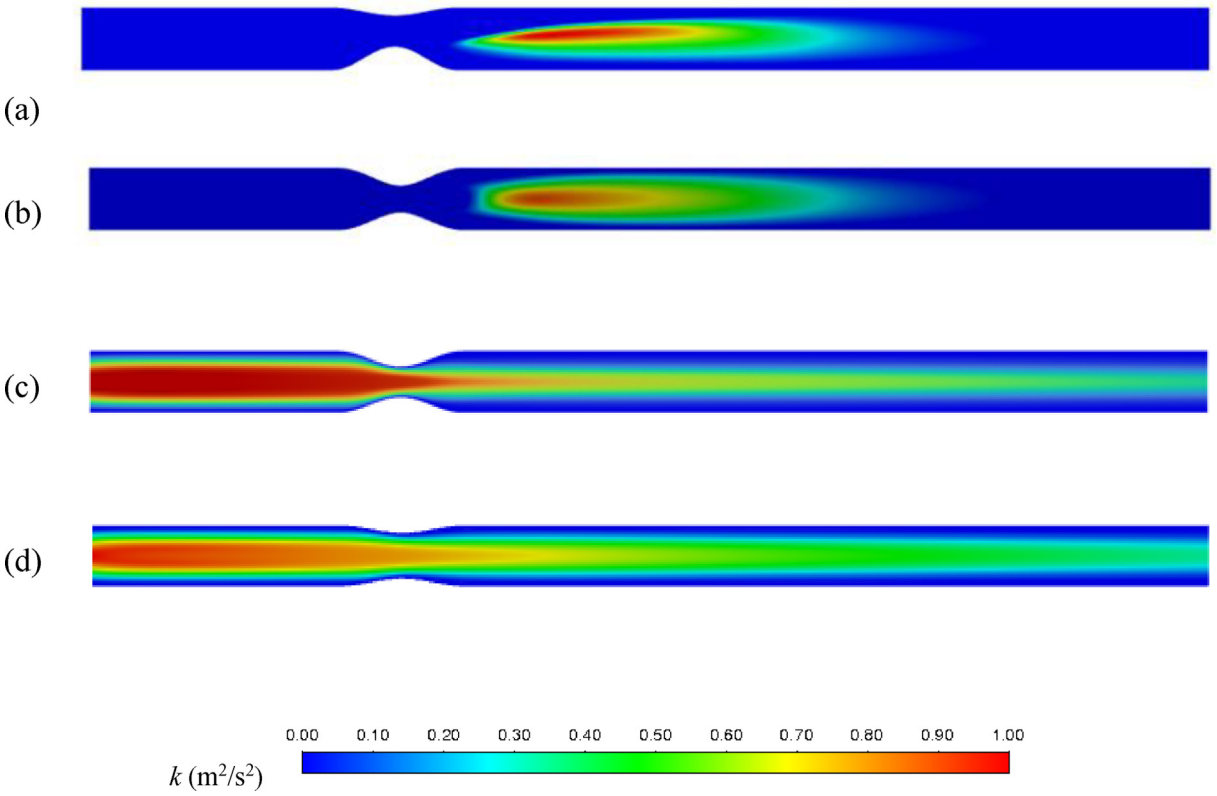

Fig. 12. Temporal-averaged of the normalized turbulent kinetic energy (TKE/TKE $_{max}$) at longitudinal sections of the computational domains: (a) x-y plane of the eccentric case, (b) x-z plane of the eccentric case, (c) x-y plane of the axisymmetric case 50%, and (d) x-y plane of the axisymmetric case 25%.

begins appearing while increasing the degree of construction, and geometry has a significant influence on bifurcations. (i.e. diameter ratio of nozzle to downstream pipe).

As shown in Fig. 8, the temporal-averaged streamwise velocity distribution observed for these cases is obtained at varying locations along with the computational domain. The streamwise velocity distribution is demonstrated on both perpendicular planes for the eccentric pipe, x-y plane (Fig. 8a) and x-z−plane (Fig. 8b), and only one plane (x-y) plane in the case of the axisymmetric case (Fig. 8c and d). As can be demonstrated from these figures (Figs. 5–8), the DoE affects the flow profile in a significant way. The velocity skewed in the eccentric case in the x-y plane with a maximum velocity of 4.69 m/s compared with the axisymmetric case, where the velocity profile is observed as a symmetric parabolic profile with a maximum velocity of 4.66 m/s. At the x-z plane for the eccentric case, axisymmetric profiles are observed but still different than that obtained from the axisymmetric case. With a comparison of three cases, eddy fluctuation appears with a higher degree of stenosis and eccentricity. For the axisymmetric case (DoS = 25%), flow is laminar and the velocity profile is symmetrically and close with each other at different cross-section cutlines. This led to a scientific definition of a fully developed velocity profile.

A high DoE (eccentric case) stenosis pipe produces a flow that resembles a wall jet. The reverse flow in the eccentric case is higher (Figs. 5a and 8a), although the flow becomes symmetrically along the x-z plane (Figs. 5b and 8b). As shown in Fig. 7, there is evidence for the separation of the boundary layer. The DoE determines where the recirculation zone, which corresponds to the area of the reverse flow, is located. The recirculation zone relates to the jet's initial deflection, growing near the centerline of the model and decreasing substantially in the lower part of the model. Eccentricity also facilitates the creation of the secondary flow and increases velocity.

In the eccentric case, the centerline velocity is found to be lower than that of axisymmetric case in the upstream stenosis region as shown in Fig. 9. However, the stream-wise velocity downstream stenosis has similar patterns of velocities as it is expected. For the axisymmetric case 25%, the peak of the velocity profile is lower than other cases around twice the time, this is relative to the ratio of diameter between cases.

3.2. Wall shear stress

In Fig. 10, the time-averaged wall shear stress (WSS) is displayed as a color contour and in Fig. 11 a line cut for axial wall shear stress, respectively. Figure 11 shows the WSS measured in several circumferential directions, represented by α, as well as the axisymmetric and eccentric cases, where α is calculated for every computational model cross-section. These figures demonstrate that, in the axisymmetric case, the WSS is distributed symmetrically. The walls of the smallest stenosis construction exhibit the maximum WSS. Axisymmetric case 25% recorded the lowest WSS with a value of 0.07 Pa. However, the eccentric case breaks the symmetry, where WSS peaks are visible at the wall in the lower half of the stenosis, where a higher shear stress is found. However, WSS in the top half of the stenosis is much lower. The WSS in the eccentric case shifts in the stenosis and downstream depending on α, in contrast to the WSS obtained in the axisymmetric model. The WSS, therefore, is found at $\alpha = 0°$, 45°, where the maximum value is obtained in the eccentric situation. At $\alpha = 135°$ and 180°, the segment of stenosis exhibits a much decreased WSS and a negative sign affected by separation phenomena. The lowest WSS is

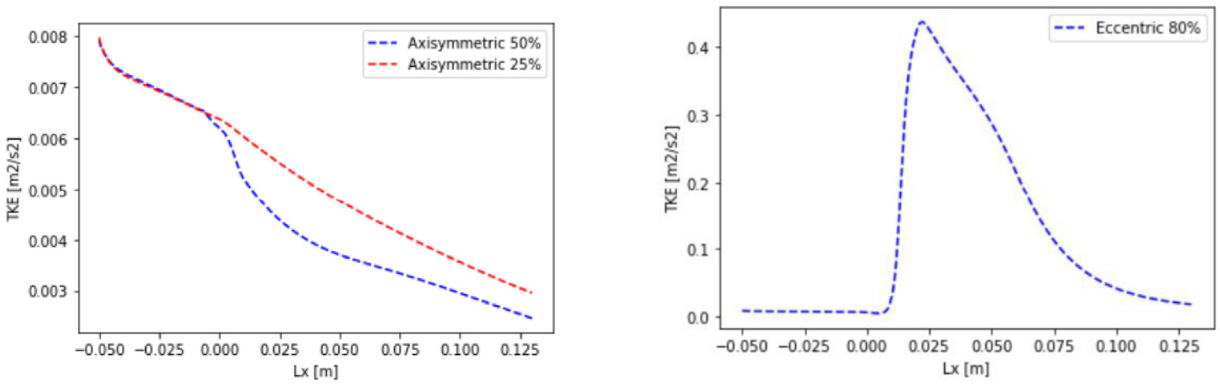

Fig. 13. Temporal-averaged normalized turbulent kinetic energy along the canter axis of the stenosis pipe. Left: axisymmetric cases. Right: eccentric at the x-y plane. A different scale has been used for each figure to show the magnitude of the TKE for each case.

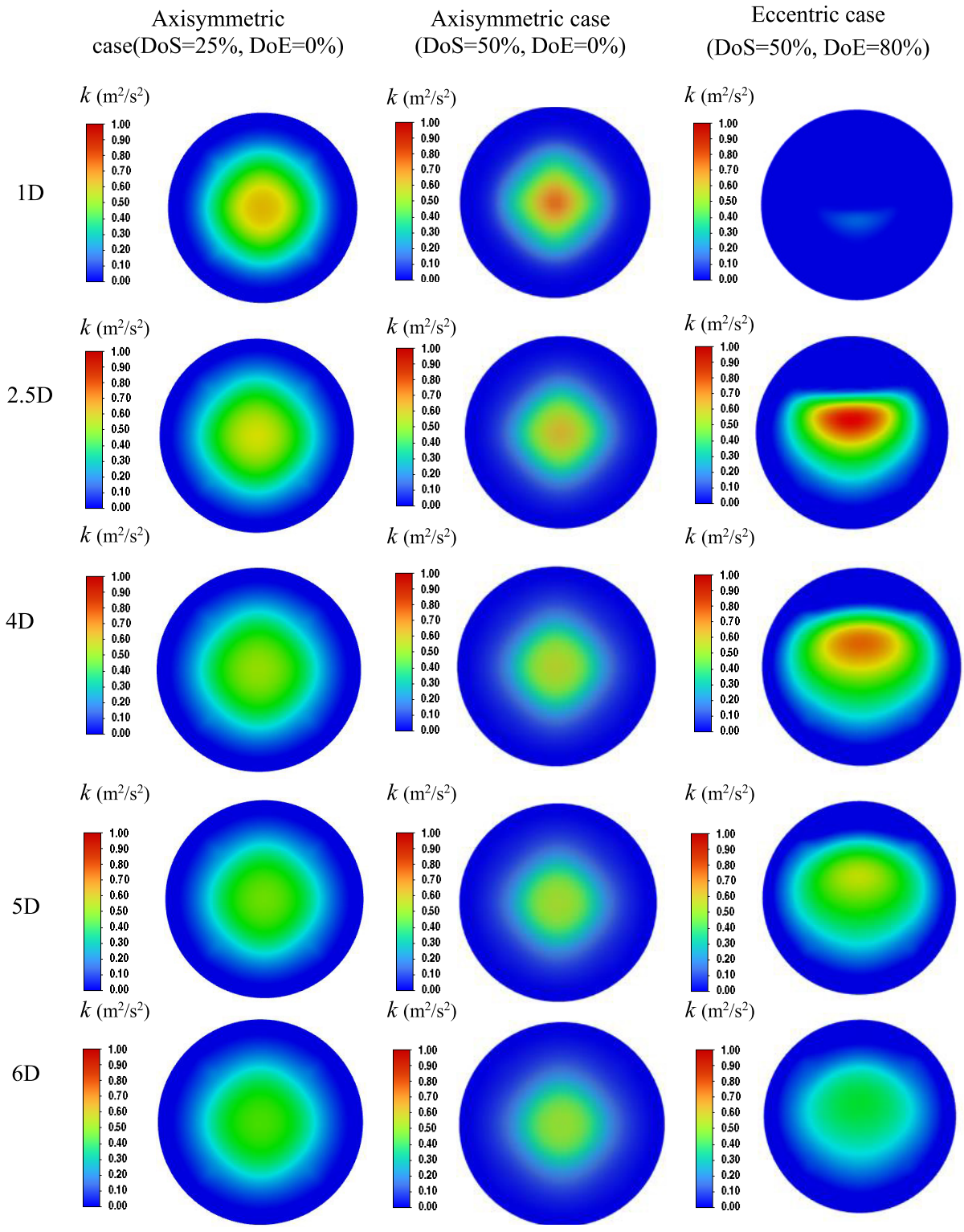

Fig. 14. Normalized turbulent kinetic energy at different cross-sections of the stenosis pipe. From top to bottom, sections at 1D, 2.5D, 4D, 5D, and 6D, respectively, from origin (x = 0).

associated with $\alpha = 180°$, as the relationship between WSS and α varies as the flow passes through the stenosis. The eccentric model has a greater peak with a higher value in the WSS at $\alpha = 135°$ and 180° further downstream, whereas the asymmetric case attained the lowest WSS.

3.3. Turbulent kinetic energy

The normalized turbulent kinetic energy TKE/TKE $_{max}$ is illustrated in Fig. 12 at the longitudinal sections of the computational domain:

$$TKE = 0.5\left(u'^2 + v'^2 + w'^2\right) \quad (6)$$

and u'^2, v'^2, and w'^2 are the root mean square of the velocity components. As shown in Fig. 12, for the eccentric case, the TKE is asymmetry in the x-y plane (Fig. 12a), whereas it is a symmetrical downstream stenosis in the x-z plane for the eccentric case (Fig. 12b). In the symmetrical case, the TKE is symmetrical and decreases gradually. It is worth noting that the maximum TKE is on the posterior side of the throat for both symmetrical cases, whereas the maximum TKE is on the lateral sides of the throat for the eccentric case. This indicates that eccentricity has modified the way of the production of TKE.

Figure 13 shows the magnitude of TKE at the line cut at the centerline of the computational domain. It can be observed that the peak value of TKE. This figure demonstrates that the magnitude of the TKE for the axisymmetric case is very small (approaches zero, TKE $_{max} = 0.008\ m^2/s^2$) and can be found in the posterior side of the throat, whereas for the eccentric case, the maximum value (TKE $_{max} = 0.48\ m^2/s^2$) is found at the later side of the throat.

The contour of the TKE at the cross sections of 1D, 2.5D, 4D, 5D, and 6D is shown in Fig. 14. From this figure, it can be observed that the largest value of the turbulent kinetic energy (TKE) is found at the midplane is 0.01 and 0.48 for the symmetric and eccentric case, respectively. It means that the increasing degree of eccentricity will increase the turbulent kinetic energy (TKE).

As shown in Fig. 15, TKE achieves a high value of 1 m^2/s^2 in the eccentric direction (x-y plane) with a low value in the axisymmetric -x-z plane. For the

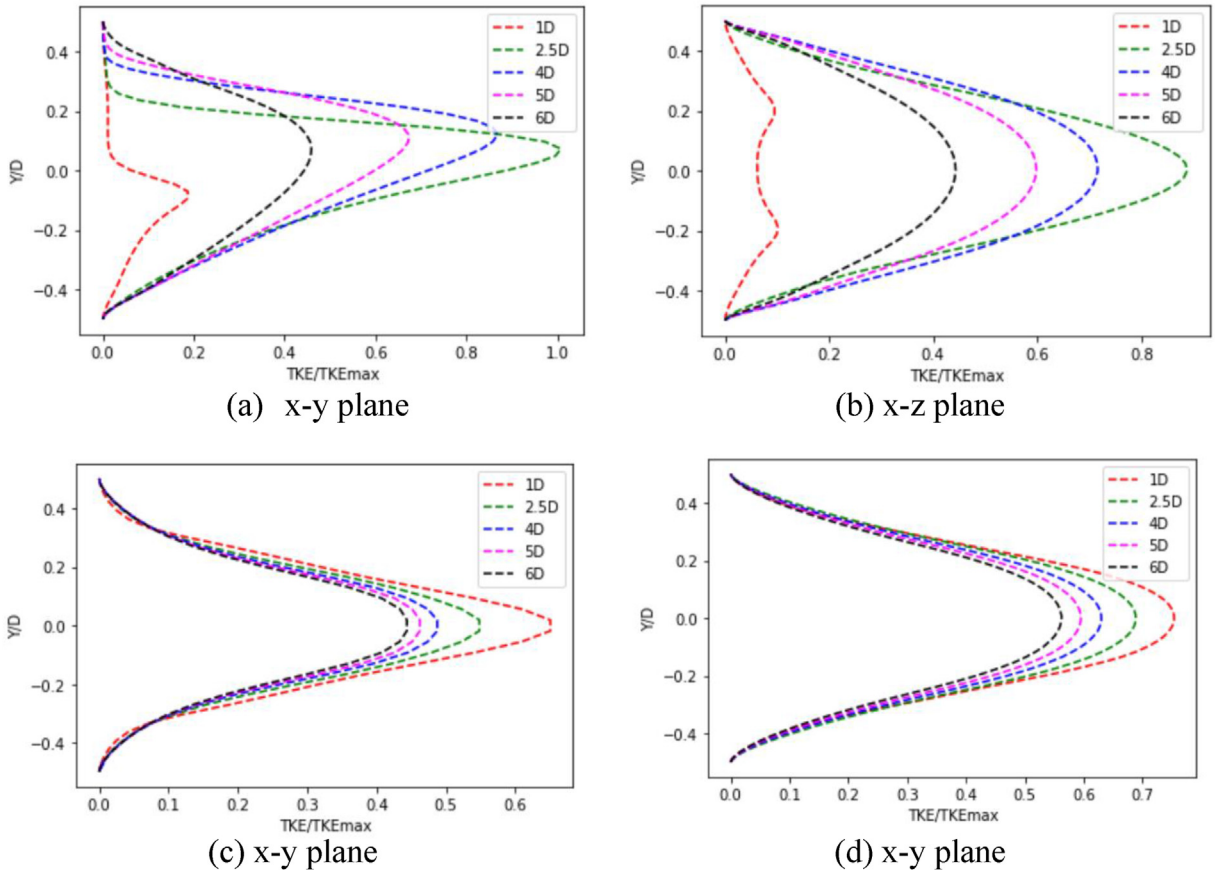

Fig. 15. Line cuts of normalized turbulent kinetic energy at different cross-sections at 1D, 2.5D, 4D, 5D, and 6D from the model's origin (x = 0):. (a) eccentric at x-y plane, (b) eccentric at x-z plane, (c) axisymmetric case 50%, and (d) axisymmetric case 25%.

a) Eccentric case b) Axisymmetric case 50% c) Axisymmetric 25%

Fig. 16. Iso-Surface Three-dimensional turbulent structured-vortices displaying with Q-criterion (Q = 5) for the three cases. Left: eccentric case. Middle: axisymmetric case 50%, and Right: axisymmetric case 25%.

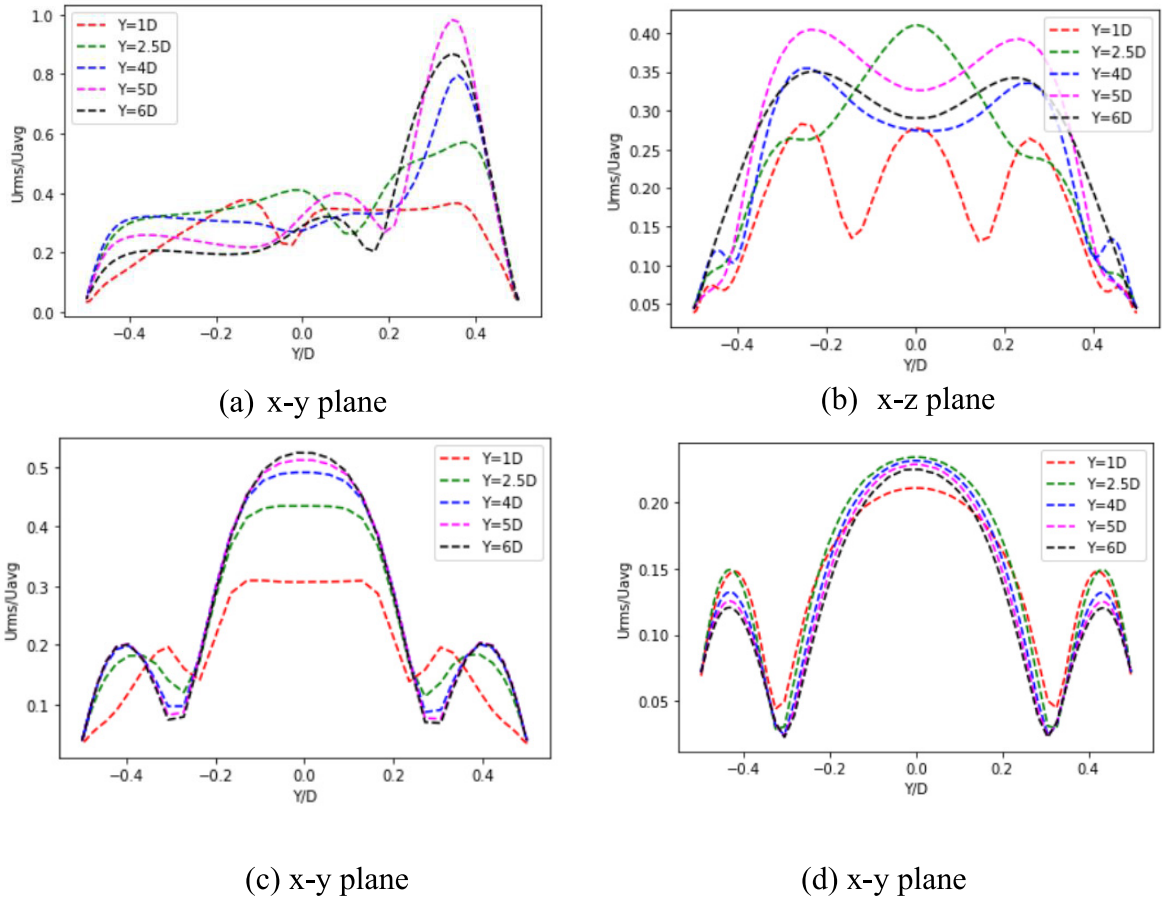

(a) x-y plane (b) x-z plane

(c) x-y plane (d) x-y plane

Fig. 17. Normalized RMS values of axial velocity at different cross sections of the stenosis pipe models measured at a distance of 1D, 2.5D, 4D, 5D, and 6D located from the origin of the computational domain (x = 0): (a) eccentric at the x-y plane, (b) eccentric at the x-z plane, (c) axisymmetric case 50%, and (d) axisymmetric case 25%.

two axisymmetric cases, there is a small difference between the value of TKE. Axisymmetric cases record the lowest value. In conclusion, axisymmetric cases have very low fluctuation. Eccentricity has a great effect on higher fluctuation.

3.4. Vortex structure

Figure 16 demonstrates the 3D vortex structures in the steady airflow fields for the three cases using Q-criterion ($Q = \frac{1}{2}$ ($\| \text{ vorticity } \|^2 - \| \text{ strain rate } \|^2$) >0). The Q-criterion proposed by Dong et al., (2019) assumes an equivalence between a vortex and complex eigenvalues of the velocity gradient tensor. The 3D vortex structures are identified by Q = 5 for the three cases. It can be seen from this figure that there are more small-scale structures in the eccentric pipe compared with that of the axisymmetric cases, particularly in the region downstream of the glottis region (stenosis region).

In summary, the observation of the flow behaviorin the stenosis pipe can be generalized for the biomedical application as follows: for the glottis region in the airway, the eccentricity will have a significant impact on the properties of the turbulent kinetic energy and the turbulent vortex in the trachea.

3.5. Root mean square

A standard flow solver (Navier–Stokes equation) can provide flow field and acoustic source term, while an acoustic solver (Light Hills or William) can provide acoustic wave propagation. Therefore, in this work, it is assumed that the turbulence/velocity fluctuations are responsible for acoustic fluctuations (Mihaescu et al., 2007). As is well known, a strong shear layer loses its symmetry forms because of the flow field passing through the stenosis region, which is representative of laryngeal constriction. In addition, the shear layer creates a powerful auditory source.

In the current work, the normalized root mean square (RMS) of the axial velocity (U_x) is calculated throughout the computational domain to assess the impact of eccentricity and different degrees of construction on the acoustics. Figure 17 shows the (U_{rms}/U_{avg}) at line cuts taken at various locations (1D, 2.5D, 4D, 5D, and 6D) along the stream direction. It can be observed that the maximum RMS is found in the eccentric case (in the x-y plane, Fig. 17a) where the maximum value of (U_{rms}/U_{avg}) in the eccentric case approaches 1, whereas the maximum value of (U_{rms}/U_{avg}) is approximately 0.53. This means that the eccentricity changes in the acoustic generation. On comparing two axisymmetric cases, DoS = 50% achieve a higher value of (U_{rms}/U_{avg}), almost twice from the value of DoS = 25% case. Velocity profiles close to each other in different cross-sections, indicated a behavior of laminar flow in axisymmetric case 25%.

3.6. Conclusions

In this work, the effects of eccentricity and degree of stenosis on the properties of the airflow field in the human respiratory tract were investigated using a simplified shape (a stenosis pipe). A turbulence model SST (k–ω) with an airflow rate of 3.5 L/min (Re = 500) was applied to examine the features of significant airflow structures, such as the jet flow and the recirculation zone, by considering both eccentric and axisymmetric cases. The turbulent kinetic energy, Q-criterion, and root mean square of the axial velocity were also discussed. From the current study, the following conclusions can be drawn:

(a) The results demonstrate that changes in the degree of eccentricity highly influence the flow in the stenosis.
(b) As much as a high degree of stenosis area (construction), flow has more fluctuation and human acoustic propagation will be harder. Higher eccentricity has a distinct vibrating mass.
(c) Eccentricity in the glottis region of the respiratory system significantly impacts the laryngeal jet. Moreover, it enlarges the size of the recirculation zone, intensifying the interaction between the jet and the recirculation zone.
(d) The magnitude value of velocity for the eccentric case increased by 4.7 m/s, while 4.67 m/s for the axisymmetric case 50%.
(e) Axisymmetric case 50% record a magnitude velocity value of 4.67 m/s, while axisymmetric case 25% record 2.49 m/s
(f) Eccentricity markedly increases the turbulence kinetic energy and root mean square of the axial velocity compared with the axisymmetric case.
(g) Turbulence kinetic energy and root mean square of the axial velocity reaches 1 m^2/s^2 in the eccentric plan, x-y plan.

3.7. Limitation and future outlook

In our future work, we aim to examine the impact of eccentricity on the flow field at higher Reynolds numbers ($500 < Re \leq 2000$) using LES to investigate the transition from laminar to turbulent flow. In addition, we conduct a more detailed study on acoustics.

There is another limitation in this research area as follows:

(a) A rigid wall is considered in this research paper but is not sufficient. Including flexible walls with realistic properties or simulating realistic airway movements could slightly alter the observed flow patterns. However, this significantly increases the computational resources needed, often ten times as much.
(b) The current study did not include the movement of vocal folds. This movement is essential for accurately predicting sound production during speech (phonation). As with other realistic simulations, including this movement would dramatically increase the amount of computing power needed under current limitations.

Author contributions

Amany Mahmoud Kamal: Conceptualization, Methodology, Validation, Software, Writing original draft. Momtaz Sedrak: Supervision. Abouelmagd Abdelsamie: Conceptualization, Supervision, Reviewing and Editing.

Ethics information

The authors declare that they have no known competing financial interests or personal relationships that could have appeared to influence the work reported in this paper.

Funding

This research did not receive any specific grant for funding.

Conflicts of interest

There are no conflicts of interest.

References

Abdelsamie, A., Koh, S. R., Janiga, G., & Thévenin, D. (2024). Transition and Acoustic Excitation of Stenotic Pipe Flows at Different Reynolds Numbers. In C. Marchioli, M. V. Salvetti, M. Garcia-Villalba, & P. Schlatter (Eds.), *vol. 31. Direct and Large Eddy Simulation XIII. DLES 2023. ERCOFTAC Series*. Cham: Springer. https://doi.org/10.1007/978-3-031-47028-8_20.

Agujetas, R., González-Fernández, M. R., Nogales-Asensio, J. M., & Montanero, J. M. (2018). Numerical analysis of the pressure drop across highly-eccentric coronary stenoses: application to the calculation of the fractional flow reserve. *BioMedical Engineering Online, 17*, 1–22.

Ahmed, S. A., & Giddens, D. P. (1983). Velocity measurements in steady flow through axisymmetric stenoses at moderate Reynolds numbers. *Journal of Biomechanics, 16*, 505–516.

Ahmed, S. A., & Giddens, D. P. (1984). Pulsatile poststenotic flow studies with laser Doppler anemometry. *Journal of Biomechanics, 17*, 695–705.

Basri, E. I., Basri, A. A., Riazuddin, V. N., Shahwir, S. F., Mohammad, Z., & Ahmad, K. A. (2016). Computational fluid dynamics study in biomedical applications: a review. *International Journal of Fluids and Heat Transfer, 1*, 2–14.

Bluestein, D., & Einav, S. (1995). The effect of varying degrees of stenosis on the characteristics of turbulent pulsatile flow through heart valves. *Journal of Biomechanics, 28*, 915–924.

Brouns, M., Verbanck, S., & Lacor, C. (2007). Influence of glottic aperture on the tracheal flow. *Journal of Biomechanics, 40*, 165–172.

Choi, Y., & Wroblewski, D. E. (1998). *Characteristics of glottis-induced turbulence in oscillatory flow: an empirical investigation*.

Cui, X., Ge, H., Wu, W., Feng, Y., & Wang, J. (2021). LES study of the respiratory airflow field in a whole-lung airway model considering steady respiration. *Journal of the Brazilian Society of Mechanical Sciences and Engineering, 43*, 1–17.

Ding, G., Choi, K. S., Ma, B., Kato, T., & Yuan, W. (2021). Transitional pulsatile flows with stenosis in a two-dimensional channel. *Physics of Fluids, 33*, 3.

Dong, X., Gao, Y., & Liu, C. (2019). New normalized Rortex/vortex identification method. *Physics of Fluids, 31*, 1.

Ferreira, J. A., Gonçalves, L., Naghipoor, J., de Oliveira, P., & Rabczuk, T. (2018). The effect of plaque eccentricity on blood hemodynamics and drug release in a stented artery. *Medical Engineering & Physics, 60*, 47–60.

Givoli, D., & Keller, J. B. (1989). A finite element method for large domains. *Computer Methods in Applied Mechanics and Engineering, 76*, 41–66.

Griffith, M. D., Leweke, T., Thompson, M. C., & Hourigan, K. (2013). Effect of small asymmetries on axisymmetric stenotic flow. *Journal of Fluid Mechanics, 721*, Article R1.

Hughes, T. J. (1995). Multiscale phenomena: Green's functions, the Dirichlet-to-Neumann formulation, subgrid scale models, bubbles and the origins of stabilized methods. *Computer Methods in Applied Mechanics and Engineering, 127*, 387–401.

Jain, K. (2020). Transition to turbulence in an oscillatory flow through stenosis. *Biomechanics and Modeling in Mechanobiology, 19*, 113–131.

Jain, K. (2022). The effect of varying degrees of stenosis on transition to turbulence in oscillatory flows. *Biomechanics and Modeling in Mechanobiology, 21*, 1029–1041.

Kleinstreuer, C., & Zhang, Z. (2003). Laminar-to-turbulent fluid-particle flows in a human airway model. *International Journal of Multiphase Flow, 29*, 271–289.

Long, Q., Xu, X. Y., Ramnarine, K. V., & Hoskins, P. (2001). Numerical investigation of physiologically realistic pulsatile flow through arterial stenosis. *Journal of Biomechanics, 34*, 1229–1242.

Longest, P. W., Hindle, M., & Choudhuri, S. D. (2009). Effects of generation time on spray aerosol transport and deposition in models of the mouth–throat geometry. *Journal of Aerosol Medicine and Pulmonary Drug Delivery, 22*, 67–84.

Mallinger, F., & Drikakis, D. (2002). Instability in three-dimensional, unsteady, stenotic flows. *International Journal of Heat and Fluid Flow, 23*, 657–663.

Mihaescu, M., Gutmark, E., Khosla, S., Scherer, R., & Fuchs, L. (2007). Flow and acoustics simulations based on LES and an acoustic analogy; an application to laryngeal airflow. In *45th AIAA Aerospace Sciences Meeting and Exhibit* (p. 919).

Samuelsson, J., Tammisola, O., & Juniper, M. P. (2015). Breaking axi-symmetry in stenotic flow lowers the critical transition Reynolds number. *Physics of Fluids, 27*, 10.

Sherwin, S. J., & Blackburn, H. M. (2005). Three-dimensional instabilities and transition of steady and pulsatile axisymmetric stenotic flows. *Journal of Fluid Mechanics, 533*, 297–327.

Timofeeva, M., Ooi, A., Poon, E. K., & Barlis, P. (2022). Numerical simulation of the blood flow through the coronary artery stenosis: effects of varying eccentricity. *Computers in Biology and Medicine, 146*, Article 105672.

Tutty, O. R. (1992). *Pulsatile flow in a constricted channel*.

Varghese, S. S., Frankel, S. H., & Fischer, P. F. (2007). Direct numerical simulation of stenotic flows. Part 1. Steady flow. *Journal of Fluid Mechanics, 582*, 253–280.

Vignon-Clementel, I. E., Figueroa, C. A., Jansen, K. E., & Taylor, C. A. (2006). Outflow boundary conditions for three-dimensional finite element modeling of blood flow and pressure in arteries. *Computer Methods in Applied Mechanics and Engineering, 195*, 3776−3796.

Wang, L., Ge, H., Chen, L., Hajipour, A., Feng, Y., & Cui, X. (2022). LES study on the impact of airway deformation on the airflow structures in the idealized mouth−throat model. *Journal of the Brazilian Society of Mechanical Sciences and Engineering, 44*, 23.

Xi, J., Si, X. A., Dong, H., & Zhong, H. (2018). Effects of glottis motion on airflow and energy expenditure in a human upper airway model. *European Journal of Mechanics - B: Fluids, 72*, 23−37.

Xie, X., Li, Y., & Xie, S. (2018). Computation of hemodynamics in eccentric coronary stenosis: a morphological parametric study. *Technology and Health Care, 26*, 229−238.

Yoganathan, A. P., Ball, J., Woo, Y. R., Philpot, E. F., Sung, H. W., Franch, R. H., & Sahn, D. J. (1986). Steady flow velocity measurements in a pulmonary artery model with varying degrees of pulmonic stenosis. *Journal of Biomechanics, 19*, 129−146.